Hydrological response of a peri-urban catchment exploiting conventional and unconventional rainfall observations: the case study of Lambro catchment

Greta Cazzaniga[1], Carlo De Michele[1], Michele D'Amico[2], Cristina Deidda[1], Antonio Ghezzi[1], and Roberto Nebuloni[3]

[1]Dipartimento di Ingegneria Civile e Ambientale, Politecnico di Milano, Milan, Italy
[2]Dipartimento di Elettronica, Informazione e Bioingegneria, Politecnico di Milano, Milan, Italy
[3]Istituto di Elettronica e di Ingegneria dell'Informazione e delle Telecomunicazioni, Consiglio Nazionale delle Ricerche, Milan, Italy

Correspondence: Carlo De Michele (carlo.demichele@polimi.it), Greta Cazzaniga (greta.cazzaniga@polimi.it)

Abstract. Commercial Microwave Links (CMLs) can be used as opportunistic and unconventional rainfall sensors by converting the received signal level into path-averaged rainfall intensity. Since in meteorology and hydrology the reliable reconstruction of the spatial distribution of rainfall is still a challenging issue, there is a wide-spread interest in integrating the precipitation estimates gathered by the ubiquitous CMLs with the conventional rainfall sensors, i.e. rain gauges (RGs) and weather radars.

Here we investigate the potential of a dense CML network for the estimation of river discharges via a semi-distributed hydrological model. The analysis is conducted in a peri-urban catchment, Lambro, located in northern Italy and covered by 50 links. A two-level comparison is made between CML- and RG-based outcomes, relying on 12 storm/flood events. First, rainfall data are spatially interpolated and assessed in a set of significant points of the catchment area. Rainfall depth values obtained from CMLs are definitively comparable with direct RG measurements, except for the spells of persistent light rain, probably due to the limited sensitivity of CMLs caused by the coarse quantization step of raw power data. Moreover, it is shown that, when changing the type of rainfall input, a new calibration of model parameters is required. In fact, after the re-calibration of model parameters, CML-driven model performances are comparable with RG-driven ones, confirming that the exploitation of a CML network may be a great support to hydrological modelling in those areas lacking a well designed and dense traditional monitoring system.

1 Introduction

Precipitation is the main downward forcing of the water cycle (Kidd and Huffman, 2011) and consequently one of the most relevant inputs in hydrological models, which are key tools in early warning systems for flood risk forecasting and mitigation (EU Water Directors, 2003). However, precipitation exhibits a significant temporal and spatial variation over a catchment area or region (Dawdy and Bergmann, 1969; Bengtsson, 2011; Parkes et al., 2013) and this is a critical aspect leading to difficulties in reconstructing a reliable rainfall field. In the past, several studies investigated the effects of spatio-temporal variability of rainfall on the hydrological model outputs (e.g., Obled et al., 1994; Bárdossy and Das, 2008; Younger et al., 2009; Arnaud

et al., 2011) proving that precipitation inputs have a marked influence on the simulated outflow hydrographs. It is also known that the reconstruction of rainfall input is more accurate as the number of rainfall measurements increases over a study area (Chen et al., 2010; Xu et al., 2013). However, because of economic or geographical factors, an adequate density of rainfall sensors is often not available.

Currently, the most common ground-based technology for rainfall measurement is the rain gauge (RG), which provides single-point measurements (New et al., 2001). In addition, high-precision ground sensors, namely disdrometers, provide size and velocity of hydrometeors (Jaffrain et al., 2011; Cugerone and De Michele, 2015). One of the major problems encountered when dealing with single-point measurements is to transfer the information to ungauged sites or to reconstruct the rainfall field over the catchment of interest. Such estimates can be performed by the use of spatial interpolation techniques. Several methods are now available, with different degrees of complexity. They can be either deterministic (e.g., the inverse distance weighting (IDW) method (Shepard, 1968) and the Thiessen polygon method (Thiessen, 1911)) or stochastic (e.g., the Kriging technique (Delhomme, 1978) and co-Kriging (Myers, 1984)). However, the outcome of these techniques is proved to be highly sensitive to the gauge density (Xie et al., 1996), depending on the temporal resolution. Specifically, the shorter the aggregation time, the more critical is the rain gauge density. Alternatively, the rainfall field at ground level can be indirectly obtained by weather radars, when available. The radar retrieves the average rainfall intensity across a volume from measurements of reflectivity through power-law formulas as the one proposed by Marshall and Palmer (1948). A recent survey of reflectivity-rainfall intensity formulas is in Raghavan (2013). Ignaccolo and De Michele (2020) and Jameson and Kostinski (2002), have argued about the purely statistical nature of the reflectivity-rainfall intensity formulas, with important consequences about their use where calibration with local data is missing. There are in addition other drawbacks associated with the use of radar reflectivity, including the problem of spurious echoes, as ground clutter (Alberoni et al., 2001; Rauber and Nesbitt, 2018), which restrict the use of radars to plain areas and the fact that the radar reflectivity provides only information about precipitable water. Recently, the dual-polarization upgrade on radars (Zhang et al., 2019; Chen et al., 2021) has added information about shape, composition, and phase of the hydrometeors. Hence, the quantitative precipitation estimation (QPE) has greatly benefited from such advancements.

For all these reasons, measuring the spatial distribution of rainfall is still an open issue, which may be tackled through the integration of conventional sensors, and/or the complement of new instruments. In this context, the use of opportunistic rainfall sensors, such as Commercial Microwave Links (CMLs), has raised considerable interest. CMLs are the point-to-point radio links connecting the base stations of a mobile network to the core infrastructure. The use of microwave links as opportunistic rainfall detectors was firstly proposed by Atlas and Ulbrich (1977). The method exploits the relationship between the rainfall intensity and the attenuation (i.e., the loss of signal power) experienced by the electromagnetic wave along the propagation path from the transmitter to the receiver. Later, Giuli et al. (1991) made use of a mesh of microwave links for the 2D reconstruction of the rainfall field, through simulation. A pioneering experimental campaign was carried out during the Mantissa project (Rahimi et al., 2003). However, at that time, the need to install ad-hoc microwave links made the technique impractical. A few years later, the scenario changed following the dramatic expansion of cellular telephony. The use of the ubiquitous CMLs connecting the base stations of cellular networks was first proposed by Messer et al. (2006). Their paper triggered many studies

that were conducted worldwide to investigate the potential of CMLs for meteorological and hydrological applications. From a hydrological point of view, CML-based rainfall products were firstly exploited by Fencl et al. (2013) to improve urban drainage modelling in a small scale (2.33 km^2) impervious catchment, in Prague (Czech Republic). Later, Brauer et al. (2016)

60 investigated the effects of the use of CML data in discharge simulations, for a natural low land catchment in the Netherlands, at small scale (6.5 km^2). A further study by Smiatek et al. (2017) used microwave links derived precipitation estimates as rainfall input in a distributed hydrological model applied to the Ammer basin (Germany), with an area of 609 km^2. In that work, authors employed the IDW method for interpolation of RG and CML rainfall data on a 100×100 m grid. Another case study was carried out on an agglomeration of cities (16 km^2) in the Czech Republic by Stransky et al. (2018), to check

65 the potential of a dense CML network for urban drainage management. Pastorek et al. (2019) assessed the impact of CML quantitative precipitation estimates (QPEs) on urban drainage modelling. The authors found that the sensitivity of CMLs is the factor which mostly affects the QPEs and that the bias on QPEs propagates throughout rainfall-runoff simulations. Moreover, they showed that the position of CMLs over the drainage area impacts the reconstruction of the runoff dynamic. In Italy, Roversi et al. (2020) conducted a validation of the CML rainfall estimates in the Po valley (northern Italy) by comparing them

70 with different data sources (RGs, the ERG5 meteorological data set, and radar products). However, to our knowledge, no one carried out a hydrological application of CML-based rainfall estimates until now.

Herein, the analysis aims at investigating and validating the potential of a CML network, located in Lombardia (northern Italy), exploited for hydrological purposes. Specifically, relying on a semi-distributed hydrological model, we assessed whether rainfall data collected by a large CML network of 50 links may be used to provide a reliable reconstruction of the hydrological

75 process in a medium-sized basin and if it is comparable with those achieved with a well designed RG network. We investigated a set of summer and autumn precipitation events (both convective and stratiform), that occurred over the Lambro catchment during the years 2019 and 2020. The analysis of events taking place in different seasons allowed us to point out some limitations of CMLs in detecting specific types of precipitation. In this work we firstly focused on the spatial interpolation of rainfall observations comparing results from conventional (RGs) and unconventional (CMLs) instruments and their combined

80 use. In fact, the issue of spatial interpolation is crucial when dealing with point (RGs) or linear (CMLs) measurements used as input into a semi-distributed hydrological model, especially when the study area is quite large (in the order of 100 km^2 or even larger). We relied on the traditional IDW method to spatially interpolate precipitation measurements/estimates from RGs/CMLs. Secondly, we implemented a semi-distributed rainfall-runoff model using three types of inputs: (1) RG measurements, (2) CML estimates and (3) the combination of RG and CML data. Given the different nature of rainfall inputs we also

85 assessed three calibrations of model parameters. We then compared results in terms of river discharge.

The remainder of this paper is structured as follows. In Sec. 2 we present the case study, the experimental setup, and the features of the networks of conventional and unconventional sensors. Section 3 includes a description of all methods implemented for the analysis and Sec. 4 reports results including a comparison of rainfall spatial interpolation carried out with the different data types and of stream flow simulations against hydrometric measurements. Discussion and conclusions are in

90 Sec. 5 and 6, respectively.
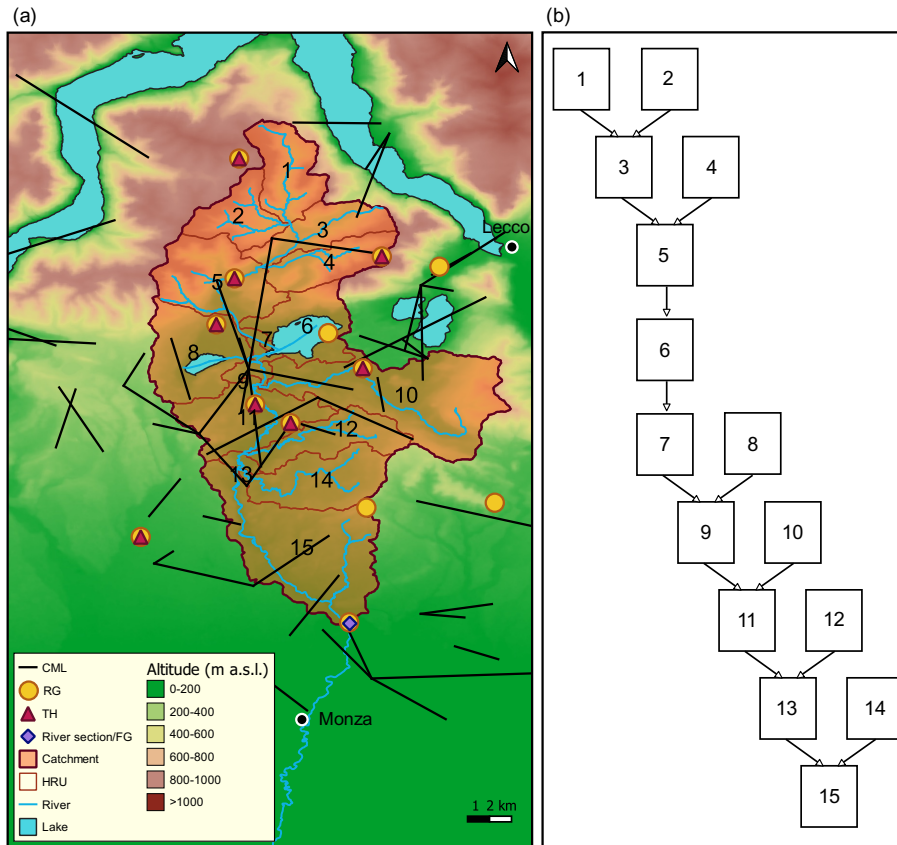
Figure 1. Case study area. Panel (a) shows the Lambro catchment, the partitioning in 15 sub-basins (HRUs), and the position of the sensors, while panel (b) reports the scheme of HRU interaction in the network. Please note that FG is the flow gauge located at the outlet section. The digital terrain model (DTM) is freely available at https://www.geoportale.regione.lombardia.it.

2 Case study and experimental setup

The case study was carried out in the Lambro catchment, a peri-urban catchment and is a Northern tributary of the Po river, shown in Fig. 1.a. It is located north of Milan metropolitan area and covers three different provinces: Como, Lecco, and Monza e Brianza. The Lambro river, at the Lesmo river section (in purple in Fig. 1.a), drains an area of $260 \ \mathrm{km}^2$ which can be mainly

95   divided in two zones, with different morphology and land use. The northern one is the Prealpine region, where the Lambro river rises, at 944 m a.s.l.. The southern one, between Pusiano lake (in sub-basin 6 in Fig. 1) and the outlet section, at 178 m a.s.l., is instead a flat area subjected to massive urbanization, which results in large impervious surfaces and, consequently, fast runoff processes with a lag time of few hours. The catchment includes the presence of two lakes: Pusiano lake (which is the biggest one) and Alserio lake (in sub-basin 8 in Fig. 1), both located in the middle part of the catchment. According to Köppen

100   (1925) climate classification, the inland northern portion of Italy belongs to the humid subtropical climate (Cfa) zone. Heavy convective precipitation cells characterize the basin, while the highest monthly rainfall accumulation occurs in spring and

autumn. The local meteorological drivers, added to urban sprawl, lead to the hydrological vulnerability of the region. In order to mitigate hydrological risk in Monza and Milan urban areas (downstream to our case study), structural works have been carried out along the Lambro river in past years. Moreover, great efforts have been made in the implementation and development of non-structural measures (e.g., Ravazzani et al., 2016; Masseroni et al., 2017; Lombardi et al., 2018), including a dense monitoring system managed by ARPA Lombardia (Regional Agency for Environmental Protection). From this, we exploited 10 min resolution rainfall depths and temperatures respectively from 13 tipping-bucket RGs and eight thermometers (THs), for years 2018, 2019, and for the first six months of year 2020. In addition, we used 10 min resolution water level measurements of a flow gauge (FG), located at the outlet section of the Lambro basin in the municipality of Lesmo. All these meteorological and hydrological data are available at https://www.arpalombardia.it. A rather dense CML network, owned by Vodafone Italia S.p.A., covers the central and southern catchment area and its surroundings. In contrast, the northernmost portion of the Lambro basin is covered by few and unevenly distributed CMLs, given that it is thinly populated and characterized by higher altitudes. The CMLs available over the area are 50. The key features of CMLs as rainfall sensors are the operation frequency and the path length. Regrouping the CMLs according to the frequency:

1. 5 links are in the frequency range [11.4,13.1] GHz, with length between 3.5 and 8 km;

2. 37 links are in the frequency range [18.8,23.0] GHz, with length between 1 and 8.5 km;

3. 8 links are in the frequency range [38.5,42.6] GHz, with length between 1.4 and 2.2 km.

We investigated 12 storm events and the associated floods, in the period June 2019–June 2020. The RG- and CML-based precipitation data sets, aggregated at hourly time scale, cover a wide range of rainy events from summer thunderstorms to low-intensity autumn events. In Table 1 we reported some features characterizing the 12 selected events, namely the initial and final date and time, accumulated precipitation averaged over 13 RG measurements, the total volume of precipitation fallen on the basin area, the 1 h maximum rain rate, the observed total flow volume, and the peak flow. We defined a storm event as the time lapse where at least one RG, available on the area, detected precipitation with possible dry intervals no longer than 5 h. An hour is considered dry when the detected rainfall depth is lower than 1 mm and wet otherwise. The beginning of the flood event is conventionally set at the hour in which the flow rate experienced a sudden deviation from the average. The end is instead set when the flow rate reverts to the initial condition, at the end of the depletion curve. According to the maximum observed rain rates, we classified events as *low rain rate* and *high rain rate*, adapting the classification reported in Met Office (2007) to our specific case study. The former group includes storm events 5, 6, 7, and 12, for which the maximum rain rate is lower than 15 mm h^{-1}, while the latter covers the remaining events with maximum rain rate higher than 15 mm h^{-1}.

For the sake of implementation of the hydrological model (see Sec. 3.2), the catchment area is divided into 15 sub-basins (as shown in Fig. 1.a), with areas ranging from 1.15 km^2 (HRU 7) to 42.6 km^2 (HRU 10). Hereinafter the sub-basins will be referred to as hydrological response units (HRUs). In particular, the semi-distributed model adopted here requires, as input data, rainfall depths estimated in the HRU centroids. The estimates were gathered through the IDW technique (see Sec. 3.3) and for each HRU a different number of sensors was exploited, according to a defined maximum distance of 10 km from the

135 HRU centroid. Figure 2 shows some features of the rainfall sensors used for spatial interpolation in each HRU: the number of exploited RGs, CMLs, and their sum, the ratio between CMLs and RGs number, the mean distance between rainfall sensors and HRU centroids, and the mean length of CMLs. Please, note that the CML-HRU centroid distance is calculated considering the CML middle point. It is also worth to mention that the number of available CMLs was less than 50 for some events due to maintenance or malfunctioning. The numbers in Fig. 2 are hence averaged over all the events. Figure 2.a highlights a significant

140 increase of the exploited CMLs from HRU 1 to 6. This could be a potential problem leading to more inaccurate estimates, at the stage of spatial interpolation, for the northern HRUs with respect to the southern ones. On the other hand, the number of RGs undergoes minor variations from one HRU to another. In Fig. 2.b we can see that the lowest ratios between CMLs and RGs correspond to HRU from 1 to 5 and the HRU 10. Moreover, Fig. 2.c shows that, considering HRUs from 1 to 9, the mean distance between sensors and HRU centroids is always higher when CMLs are considered. The opposite trend, with a

145 single exception for HRU 12, occurs for HRUs located further downstream. Lastly, the mean CML length, in Fig. 2.d, has a decreasing trend from upstream to downstream.

Table 1. Details of the 12 events considered. On the left side, date, time, cumulative precipitation, precipitation volume, and 1 hour maximum rain rate for the 12 storm events. On the right side, date, time, flow volume, and peak flow of the corresponding flood events. Here, LT stands for local time.

ID event	Storm event				Flood event		
	Date and Time (LT)	Cumulative precipitation (mm)	Volume (m^3 10^{12})	Max rain rate (mm h^{-1})	Date and Time (LT)	Volume (m^3 10^6)	Peak flow (m^3 s^{-1})
1	22 Jun 2019, 06:00 22 Jun 2019, 15:00	40.5	10.5	37.6	22 Jun 2019, 08:00 22 Jun 2019, 23:00	0.9	46.3
2	14 Jul 2019, 22:00 16 Jul 2019, 03:00	63.6	16.5	49.0	22 Jun 2019, 08:00 16 Jul 2019, 23:00	2.4	48.2
3	05 Sep 2019, 01:00 09 Sep 2019, 10:00	68.7	17.9	36.6	05 Sep 2019, 21:00 11 Sep 2019, 23:00	1.9	29.7
4	18 Oct 2019, 17:00 22 Oct 2019, 12:00	108.4	28.2	35.2	19 Oct 2019, 00:00 24 Oct 2019, 23:00	6.2	54.8
5	14 Nov 2019, 19:00 16 Nov 2019, 17:00	34.5	8.97	12.6	15 Nov 2019, 04:00 17 Nov 2019, 04:00	2.9	25.7
6	17 Nov 2019, 01:00 17 Nov 2019, 19:00	25.6	6.66	6.4	17 Nov 2019, 10:00 19 Nov 2019, 03:00	3.8	34.7
7	18 Nov 2019, 23:00 20 Nov 2019, 00:00	27.9	7.26	4.0	19 Nov 2019, 04:00 21 Nov 2019, 23:00	6.6	31.0
8	14 May 2020, 20:00 16 May 2020, 07:00	64.2	16.7	31.0	14 May 2020, 22:00 17 May 2020, 02:00	3.5	50.1
9	03 Jun 2020, 16:00 05 Jun 2020, 04:00	79.9	20.8	24.8	03 Jun 2020, 18:00 05 Jun 2020, 19:00	3.5	30.4
10	07 Jun 2020, 08:00 08 Jun 2020, 02:00	42.1	10.9	29	07 Jun 2020, 15:00 08 Jun 2020, 19:00	3.4	65.8
11	08 Jun 2020, 17:00 09 Jun 2020, 19:00	32.2	8.37	22.8	08 Jun 2020, 20:00 10 Jun 2020, 01:00	3.5	65.7
12	10 Jun 2020, 11:00 11 Jun 2020, 07:00	16.5	4.29	7.4	11 Jun 2020, 02:00 11 Jun 2020, 15:00	1.3	31.1
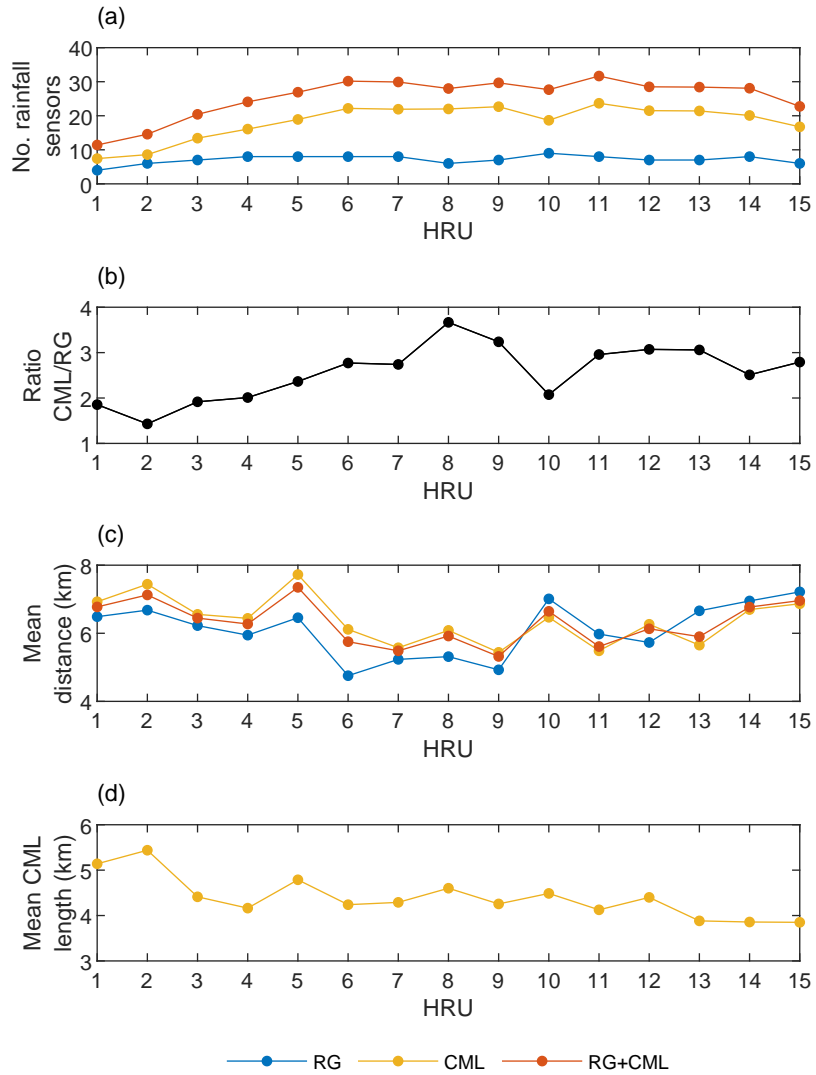
Figure 2. From panel (a) to (d): number of rainfall sensors used for spatial interpolation in each HRU centroid, ratio between the number of RGs and CMLs, mean distance between rainfall sensors and HRU centroids, and CML mean lengths.

3 Methods

In this section we firstly describe the algorithms of data processing. While for conventional sensors (RGs, THs, and FG) the procedure is simple, it is not straigthforward to extract quantitative rainfall information from CML raw data, which are generated for network monitoring purposes. Second, we discuss the semi-distributed hydrological model and its calibration/validation procedures. Finally, we illustrate the methods of spatial interpolation of RG- and CML-based rainfall data.

3.1 Data processing

Conventional sensors (rain gauges, thermometers, and flow gauge)

Raw data from RGs, THs and the FG were firstly processed to correct invalid measurements (missing data and outliers), which account for less than 1% in the period January 2018–June 2020. The process is different depending on the type of measurement. Invalid RG data were replaced interpolating valid observations from the nearby sensors by the IDW algorithm. Invalid TH data, as well as invalid FG measurements, were instead replaced by linear interpolation. After data correction, the 10 min raw data were resampled to hourly time scale. Lastly, water level observations were converted into river discharge measurements by using the rating curves, validated by the Hydrographic Office of ARPA Lombardia.

Commercial Microwave Links

CML raw data are minimum and maximum values of the transmitted and received power levels (TSL and RSL, respectively) every 15 min. Microwave links of mobile networks are usually two-ways and provide dual-frequency operation. The CML data set used here has two to four channels available for every link, which allows us to deal with missing or invalid data appearing sometimes over a certain channel. Procedures for the conversion of RSL into rainfall rate have been detailed by several authors (e.g., Schleiss and Berne, 2010; Fenicia et al., 2012; Overeem et al., 2016). As the format of the available CML data is the same as in Overeem et al. (2016), we built from the procedure outlined there. Specifically, data processing went through the following steps: (1) identification and removal of outliers and artifacts (i.e., occasional spikes, which are not caused by rain); (2) classification of each 15 min time slot into dry or wet (i.e., rainy) by thresholding the difference between maximum and minimum RSL values; (3) estimation of the baseline, i.e., RSL in the absence of rain; (4) calculation of total signal attenuation as the difference between the baseline and the actual RSL; (5) identification and subtraction of the components of total attenuation not due to rainfall (e.g. wet antenna attenuation); (6) conversion of rain attenuation into rainfall intensity. Details of the major processing steps are discussed in the following.

Dry/wet classification at step (2) is required by subsequent steps (3) and (5). First, RSL fades are identified by a robust method based on a lower and an upper threshold: all RSL samples below the upper threshold with at least one point below the lower threshold are retained. Then, each CML is given a score equal to the product of the binary outcome (0/1) of thresholding by the inverse of its sensitivity to rainfall, the latter depending on CML frequency and length. Finally, a CML is flagged as wet if the aggregate score of the CML itself and of all its neighbors exceeds 0.5, otherwise it is dry. Two CMLs are neighbors if

they fulfill any of the following conditions: (1) they have a terminal in common, (2) their paths intersect, and (3) their distance is less than a defined maximum value. The baseline on step (3) is obtained through a windowing algorithm. An N-sample window is centered around each sample of the RSL time series. If enough samples in the window are dry, the baseline value in the center of the window is the average of minimum and maximum RSL. Once the entire time series has been processed, the baseline missing points are obtained by linear interpolation. In step (5), it is assumed that wet antenna attenuation is the only relevant component of total path attenuation not due to rain. This contribution is subtracted from total attenuation using the model proposed by Schleiss et al. (2013), which predicts an exponential increase of attenuation during the wetting transient, a constant value while raining and an exponential decrease during the drying transient. The input parameters of the model, that are the duration of the initial transient and the maximum value of wet antenna attenuation, are 900 s and 2 dB, respectively. They were determined analyzing a set of RSL and TSL time series sampled every 10 s, which were made available for a few CMLs. The relationship between rain attenuation per unit path length γ_R (dB km^{-1}) and rainfall intensity R (mm h^{-1}) is usually modelled by the following power-law function:

$$\gamma_R = \kappa R^{\alpha}. \tag{1}$$

The coefficients κ and α have been tabulated by the International Telecommunication Union as a function of signal frequency and polarization (ITU-R P.838-3, 2005). In principle, the $\gamma_R - R$ relationship is dependent on the microphysics of rain as well, hence κ and α should be calibrated, provided that the characteristics of precipitation are known in the climatic area where CMLs are deployed. In this work, raindrop size distribution data gathered from disdrometers were used to calculate the optimum value of κ and α coefficients following the procedure outlined in Luini et al. (2020). In the available CML data format, only the two extreme values of TSL and RSL are saved in every 15 min window. Therefore, if the average rainfall rate has to be estimated, for instance to calculate hourly accumulations, it is necessary to derive it from the extremes. To this aim, TSL and RSL time series sampled each 10 s were made available for a subset of CMLs during some of the events considered here and processed as shown in Nebuloni et al. (2020). Average, min and max rainfall rate within 15 min windows were calculated from the 10 s time series and the following unbiased estimator of the average rainfall rate was derived:

$$R_{\mathrm{MIN-MAX}} = \frac{1}{1.14} \frac{R_{\mathrm{MIN}} + R_{\mathrm{MAX}}}{2}. \tag{2}$$

Two aspects of the above procedure deserve more discussion. First, the available RSL sequence have a coarse 1 dB quantization step, which produces a zero-mean random error with rectangular distribution and limiting values equal to ± 0.5 dB ($\pm 12\%$ when the power is measured on a linear scale). It turns out that it is impossible to distinguish between rain and quantization-induced noise below a certain rainfall intensity threshold. Figure 3 shows the minimum detectable rainfall intensity without ambiguity as a function of the CML path length with the CML frequency as parameter. The square markers correspond to the 50 CMLs in the study area divided into three groups according to their frequency band. Continuous lines are drawn at three reference frequencies as well. Moreover, quantization affects the accuracy of rainfall intensity estimates. The accuracy of instantaneous measurements (at the 95% confidence level) is within 20% if the rainfall intensity exceeds 3 mm h^{-1} for the link with the most favorable combination between length and frequency. However, in the worst case, the above accuracy

is achieved only if the rainfall intensity is above $10~\mathrm{mm\,h^{-1}}$. The only way to mitigate quantization effects is to average in time. Second, it is assumed that the rain attenuation measured over a CML of length L, is L times the attenuation per unit path length in Eq. (1), which implies that rain is considered uniform along the path. The effect of the inhomogeneity of precipitation can be relevant as CML paths range from about $1~\mathrm{km}$ to nearly $9~\mathrm{km}$ (Fig. 3). Some authors proposed to retrieve the spatial distribution of the rainfall field across the measurement area by processing all the CML data together, for instance through tomographic techniques. In this work, a simpler approach is used. Each CML is considered independently of the others and the corresponding rainfall measurement is given a weighting coefficient dependent on the distance between its midpoint and the point where rainfall has to be estimated, as discussed in Sec. 3.3.

In order to validate the rainfall estimates provided by CMLs, we compared the accumulated rainfall during each of the events in Table 1 with direct RG measurements. In this respect, we highlight that CMLs carry out path-averaged rainfall measurements. Hence, it is not straightforward to validate CML-based outcomes with measurements from rain gauges, that are single-point sensors, unless ad hoc-deployments are used, which is not the case of this study. Here, CMLs and RGs are associated according to their mutual distance. Each RG is given a different weight depending on its position with respect to an associated CML, as follows: the CML path is divided into short segments, the distance between the RG and each CML segment (approximated by its midway point) is calculated, and all the above distances are averaged. The number coming out of this calculation takes into account the relative position of the CML and of the RG as well as CML length. Finally, the rainfall accumulated from the set of RGs associated with a given CML is calculated by the IDW method using the average CML–RG distance. The scatter plot between CML– and RG–based accumulated rainfall is plotted in Fig. 4 for the eight high-intensity (panel (a)) and the four low-intensity events (panel (b)), respectively. Only RGs within $5~\mathrm{km}$ (average distance) from a CML are considered. During high-intensity events, there is a good match between CML and RG estimates, whereas CMLs exhibit an evident underestimation (more than 30% on the average) in the case of low-intensity events. This pattern can be explained
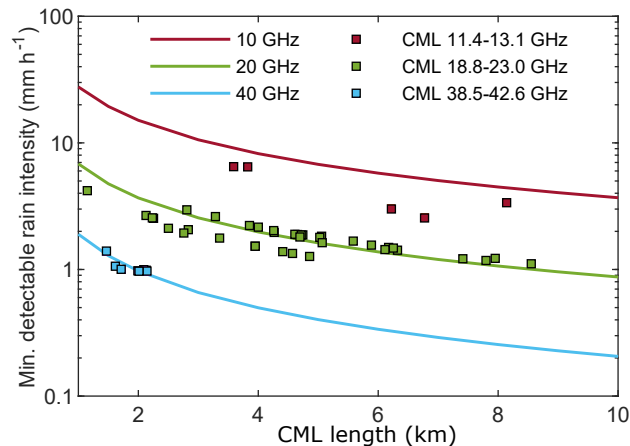
Figure 3. Minimum detectable rainfall intensity as a function of path length for link frequencies of 10, 20, and 40 GHz, assuming a 1 dB quantization step on RSL. Squares represent the frequency and length of the 50 available CMLs in the study area.
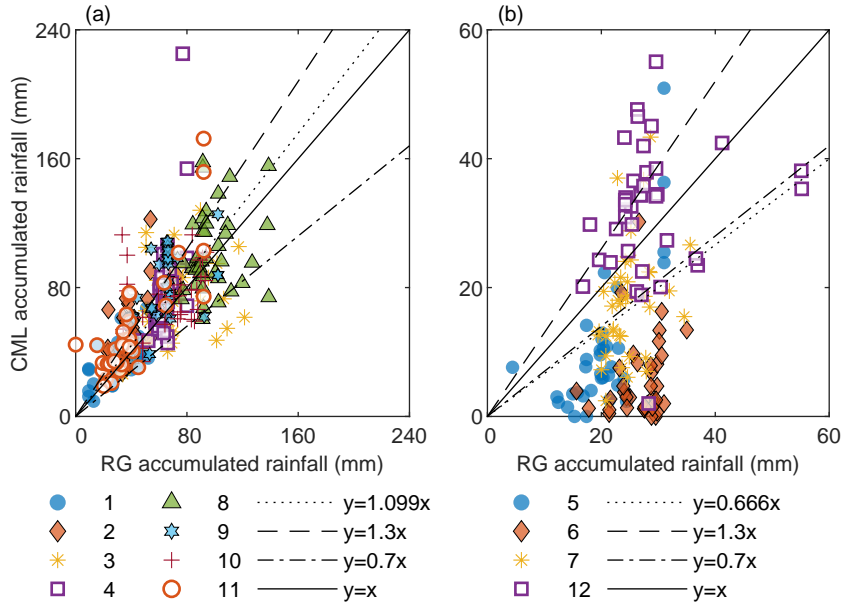
Figure 4. Accumulated rainfall during (a) *high rain rate* events and (b) *low rain rate* events: CMLs against nearby RGs. The best fit of data, the ±30% bounds, and the 45° line are shown as well. In the legend, numbers refer to the storm events and markers are the selected CMLs.

by the lack of sensitivity of CMLs to low rainfall intensities due to signal quantization. In Appendix A we present a further local comparison, between CML and nearby RGs on rainfall time series.

3.2 Hydrological model

235 We used a semi-distributed rainfall-runoff model, at an hourly time scale. As shown in Fig. 1, the catchment area is divided into 15 HRUs, which are considered meteorologically, geologically, and hydrologically homogeneous. The model parameters are hence set at HRU scale.

The river discharge at time t, $Q(t)$, in HRU's outlets is calculated as the sum of two main components

$$Q(t) = Q_s(t) + Q_g(t), \tag{3}$$

240 where Q_s is the contribution given by the surface runoff R^*, i.e., the portion of rainfall not infiltrated into the soil, an Q_g is the groundwater discharge.

The computation of R^* (in mm) relies on the SCS-CN method (US Department of Agriculture Soil Conservation Service, 1985):

$$R^* = \frac{(P - I_a)^2}{P - I_a + S}, \tag{4}$$

245 where $P \geq I_a$ (in mm) is the rainfall depth, S (in mm) is the maximum soil potential retention, and I_a (in mm) is the initial abstraction (calculated as a percentage, 20%, of S). According to USDA-SCS guidelines, the soil moisture condition antecedent

to a storm event is classified depending on the value of the five-day antecedent rainfall. Here, we account for the actual soil moisture in a dynamical way, as proposed in the AnnAGNPS model (Bingner and Theurer, 2005) and also implemented in Ravazzani et al. (2007). In particular, the value of $S(t)$ is updated as a continuous function of the degree of soil saturation $\epsilon(t)$ (-)

$$S(t) = S_I \cdot \left\{ 1 - \left[\frac{\epsilon(t)}{\epsilon(t) + \exp(W_I - W_{II} \cdot \epsilon(t))} \right] \right\}, \tag{5}$$

where the weights W_I (-) and W_{II} (-) are defined as follows

$$W_I = \ln \left[\frac{1}{1 - S_{III}/S_I} - 1 \right] + W_{II}; \tag{6}$$

$$W_{II} = 2 \cdot \left[\ln \left(\frac{0.05}{1 - S_{II}/S_I} - 0.5 \right) - \ln \left(\frac{1}{1 - S_{III}/S_I} - 1 \right) \right], \tag{7}$$

where S_I, S_{II}, S_{III} are the retention parameters associated with the curve numbers CN_I, CN_{II}, and CN_{III}, respectively. Finally, $\epsilon(t)$ is calculated as

$$\epsilon(t) = \frac{\theta(t) - \theta_{res}}{\theta_{sat} - \theta_{res}}, \tag{8}$$

where θ_{sat} (-) is the soil moisture at saturation conditions and θ_{res} (-) is the residual soil moisture.

To calculate Q_s at time t, the runoff is routed to the HRU's outlet, representing each HRU as a linear reservoir model (Dooge, 1973):

$$Q_s(t) = \int_0^t a \cdot r^*(\tau) \cdot A \cdot T_{lag}^{-1} \cdot \exp \left(-\frac{t - \tau}{T_{lag}} \right) d\tau, \tag{9}$$

where $a = 10^{-3}$ m mm^{-1} is a conversion factor, r^* is the surface runoff rate (in mm s^{-1}), A (in m^2) is the HRU area, and T_{lag} (in s) is the lag time calculated as 0.6 times the concentration time, T_c, for average natural watershed conditions and an approximately uniform distribution of runoff according to Mockus (1957) and de Simas (1996). The calculation of T_c, in each HRU, relies on the formula proposed by Ferro (2006).

The portion I (in mm) of total rainfall that infiltrates in the shallower layer of soil can either be lost by evapotranspiration, ET (in mm), or by percolation, D (in mm). Potential evapotranspiration (PET) is here calculated by the Hargreaves and Samani (1985) equation, which requires temperature data. The actual evapotranspiration (ET) is computed as a fraction of PET following Ravazzani et al. (2015). The water balance equation, referred to the shallower layer of soil with depth z (in mm) at time t, is formulated as

$$\theta(t) = \theta(t - 1) + \frac{I(t - 1) - D(t - 1) - ET(t - 1)}{z}, \tag{10}$$

where θ (-) is the actual soil moisture. $D(t)$ is the drainage flux calculated as

$$D(t) = c \cdot K_{sat} \cdot \epsilon(t)^{\frac{2 + 3B}{B}}, \tag{11}$$

where $c = 3.6 \cdot 10^6$ (in $\mathrm{mm\,s\,m^{-1}}$) is a conversion factor, K_{sat} (in $\mathrm{m\,s^{-1}}$) is the hydraulic conductivity at saturation, and B is the Brooks-Corey index (Brooks and Corey, 1964). Finally, $Q_g(t) = a \cdot \Delta T^{-1} \cdot D(t) \cdot A$, with $\Delta T = 3600$ s. The interaction among HRUs is presented in series or in parallel reservoirs, according to the development of the river network, as exhibited in Fig. 1.b. CN values were taken from https://www.isprambiente.gov.it while θ_{res}, θ_{sat}, and B parameters were taken from Maidment (1993). K_{sat} and z are instead calibrated, as reported below.

Calibration and validation of the hydrological model

The hydrological model was calibrated using, as input, the hourly rainfall depths from the RG network in Fig. 1.a. The chosen period for calibration is 1 January 2019–31 December 2019. We tested different combinations of the two parameters, K_{sat} and z, and we selected the combination maximizing the Nash and Sutcliffe (1970) efficiency (NSE). Concerning K_{sat} we tested the values reported in Maidment (1993) multiplied by several different powers of 10, $\{10^{-2}, 10^{-1}, 10^0, 10^1, 10^2\}$. The values of K_{sat} taken from the literature are different depending on the type of soil characterizing each HRU. With regard to z, we tested all the values inside the range [10 cm, 3 m], with a 10 cm step. The parameter validation was carried out over two non-consecutive six-months periods: 1 July 2018–31 December 2018 and 1 January 2020–30 June 2020. The NSE value is 0.69 for the calibration and 0.56 for the validation, respectively. Please note that the calibrated parameters provide a NSE larger than 0.5 for the overall one-year validation period, which is the minimum value recommended by Moriasi et al. (2007) to consider a simulation reliable.

It is also worth noting that the calibration and validation steps were particularly troublesome due to the presence of the Cavo Diotti dam, which artificially regulates the outflow of Pusiano lake during flood events.

3.3 Spatial interpolation of rainfall data

Several methodologies have been proposed and applied for the spatial interpolation of rainfall measurements retrieved from CMLs (e.g., Fencl et al., 2013; Overeem et al., 2013; D'Amico et al., 2016; Haese et al., 2017; Chwala and Kunstmann, 2019; Graf et al., 2020; Eshel et al., 2021). Here, we exploited the simple and robust IDW method (Shepard, 1968) for both RG and CML measurements. According to the IDW method, given n measurements $\{u(\mathbf{x}_1), ..., u(\mathbf{x}_n)\}$ at given points $\mathbf{x}_i$, with $i = 1, ..., n$ the interpolated value u, in $\mathbf{x}$, is calculated as

$$u(\mathbf{x}) = \begin{cases} \frac{\sum_{i=1}^{n} w_i' \cdot u(\mathbf{x}_i)}{\sum_{i=1}^{n} w_i'} & \text{if } d(\mathbf{x}_i, \mathbf{x}) \neq 0 \text{ for all } i; \\ \\ u(\mathbf{x}_i) & \text{if } d(\mathbf{x}_i, \mathbf{x}) = 0 \text{ for some } i, \end{cases} \tag{12}$$

with

$$w_i' = \frac{1}{d(\mathbf{x}_i, \mathbf{x})^{\gamma}}, \tag{13}$$

where $d(\mathbf{x}_i, \mathbf{x})$ is the distance between the measuring point $\mathbf{x}_i$ and the coordinates of HRU's centroid $\mathbf{x}$, and $\gamma > 0$. The number of contributing measurements n is the one within a distance d_{max} from the query point. We identified the appropriate value
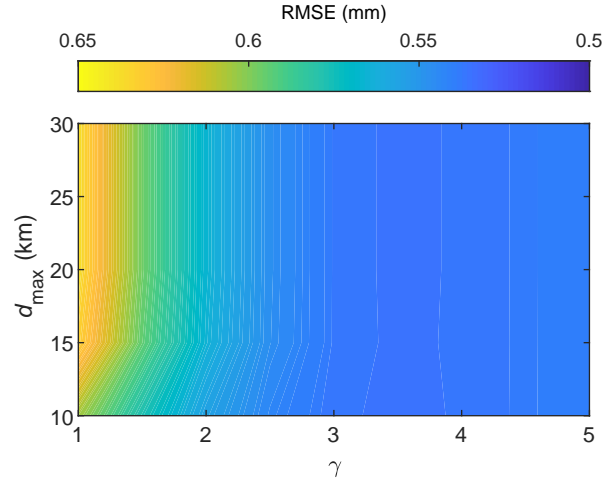
Figure 5. IDW calibration based on RGs: RMSE between observed and simulated rainfall depths, for different values of γ and d_{max}, from Eq. (13).

for γ and d_{max} by leave-one-out cross validation. We estimated the precipitation, at each RG point, from the remainder of RGs at a distance smaller than d_{max}, and calculated the Root Mean Square Error (RMSE) between observations and estimates. The process was repeated for several values of γ and d_{max}. We set a minimum d_{max} value equal to 10 km, to have at least

305   one neighbour available for every considered RG. To this aim, we exploited a larger set of 38 RGs (including the 13 RGs in Fig. 1.a) located on a wider area compared to the Lambro catchment and we used data from January 2018 to June 2020. The resulting RMSE distribution as a function of d_{max} and γ is reported in Fig. 5. We observe that the choice of d_{max} has a rather marginal effect on the estimates if $\gamma \geq 2$. The minimum RMSE is achieved when γ is slightly above 3. We therefore chose $\gamma = 3$. Moreover, we selected $d_{max} = 10$ km, which provides the best RMSE when $\gamma = 3$. To spatially interpolate CMLs rain

310   rates, we handled them as *virtual* RGs, assuming the rainfall measurement is collapsed into the midpoint of the CML path. Again we used IDW method and the same values of γ and d_{max} as above. In addition of considering only RGs, or only CMLs, we accounted for the integration of RGs and CMLs measurements. In the following, we will refer to this option as CML+RG.

4   Results

The results are presented in the following two subsections. Sec. 4.1 provides a comparison of rainfall depths interpolated at

315   the HRU centroids, by using data either from conventional or opportunistic sensors. Both accumulated rainfall values and hourly rainfall depths are considered at basin and sub-basin scale, for the 12 events. We therefore investigate whether there are some critical issues that might help to explain differences in the rainfall-runoff model outputs. Sec. 4.2 analyzes discharge performances, by comparing RG-, CML-, and RG+CML-driven simulations with the observed flow rates.

4.1 Comparison between RG and CML rainfall data in each HRU

320 Figure 6 shows the scatter plot of the rainfall accumulated at the end of each of the 12 storm events and averaged over the entire catchment area. Yellow markers are CML against RG rainfall depths, while in orange are CML+RG against RG rainfall depths. On the one hand, for all the *low rain rate* events (squares), estimates from CMLs and from CMLs+RGs are lower than the ones from RGs. On the other hand, CML (and CML+RG)-estimates of *high rain rate* events, are in agreement (with either lower and higher values) with the RG-based ones, with the only exception of event 3. From a more general perspective, the 325 two regression lines indicate a good agreement between the two sets of sensors.
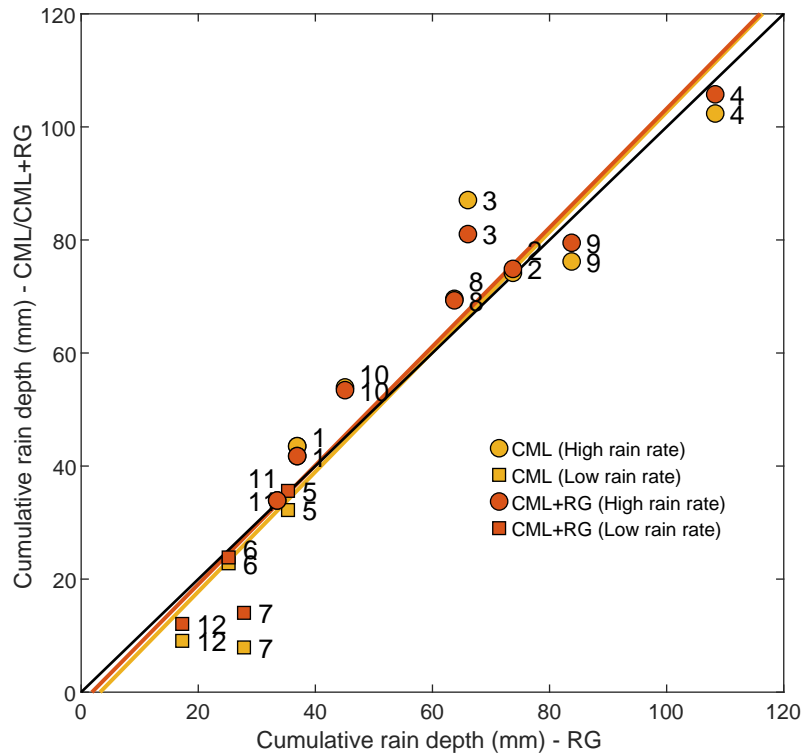
Figure 6. Rainfall depths, averaged over the catchment area and accumulated at the end of each of the 12 events. The number next to the markers refer to the ID event while the two different markers, circles and squares, respectively stand for *high rain rate* and *low rain rate* events. The black line represents the 1:1 line of perfect matching between rainfall depth estimates from RGs and from CMLs (yellow) or from the combination of RGs and CMLs (orange). Yellow and orange lines are the corresponding regression lines.

We further assessed CML and RG rainfall estimates on the hourly time scale and on the sub-basin spatial scale by calculating the relative error of CML estimates with respect to RG ones, assuming the latter as benchmark, for the hourly rainfall depths

inferred in the 15 HRU centroids. The relative error ΔE is evaluated as:

$$\Delta E = \frac{R_{CML} - R_{RG}}{R_{RG}}, \tag{14}$$

330   where R_{CML} and R_{RG} are the 1 hour rainfall depths estimated in each HRU centroid, respectively from CMLs and RGs. For the calculation, we only considered wet hours ($R_{RG} \geq 1$ mm in HRU centroids), relying on a data set of 2061 values. Hence, when the CML estimate yields 0 and the RG estimate is greater than 0 (*false negative*), the relative error is -1. Figure 7 shows a 2D histogram representing the count of rain hours falling in a given range of RG-estimated rainfall depths and in a given range of relative errors. The increasing spread of ΔE values with respect to the decrease of the RG-based rainfall depths is due to the

335   greater uncertainty of CMLs in detecting low rain rates. If the RG-based rainfall depth is smaller than 3 mm, only 30% of ΔE values falls in the range [-0.4, 0.4], whereas if it is larger than 3 mm, the percentage increases up to nearly 70%. Moreover, for the lowest rainfall depths there are fewer negative values of ΔE as we set to zero all the CML rain rate estimates lower than the sensitivity of the link itself. The high count related to $\Delta E = -1$ and RG-based rainfall depths < 5mm is due to the occurrence of *false negatives*.
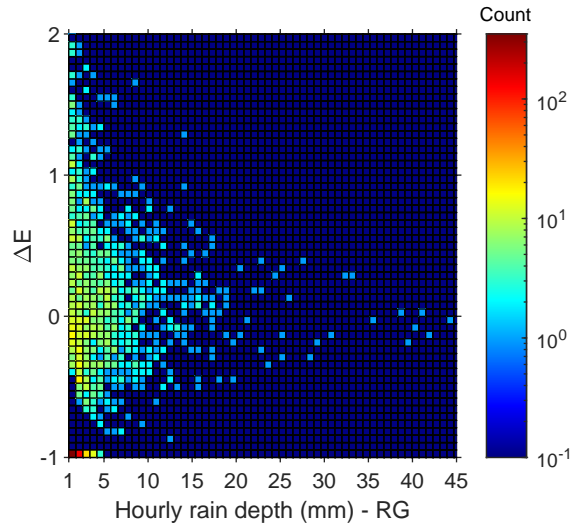
Figure 7. 2D histogram of hourly rainfall depth from RGs and ΔE. The colour of each equally spaced 2D bin represents its height, which is the count of data falling in the bin. The scale bar has a logarithmic scale and the dark blue bins correspond to 0 counts. Values of ΔE equal to -1 represent false negatives.

340   We therefore focused on the CML hourly wet-dry classification, inferred in HRU centroids, again considering RG estimates as benchmark. We recall that dry hours are those in which the detected rainfall depth is lower than 1 mm and vice versa for wet hours (see also Sec. 2). Figure 8 depicts box plots of the percentage of *false negatives* and *false positives* for *low rain rate* and *high rain rate* events. In contrast to a *false negative*, a *false positive* occurs when an hourly slot is classified as wet by CMLs and dry by RGs. The two box plots on the left were obtained relying on 120 values which are the percentages of *false positive*
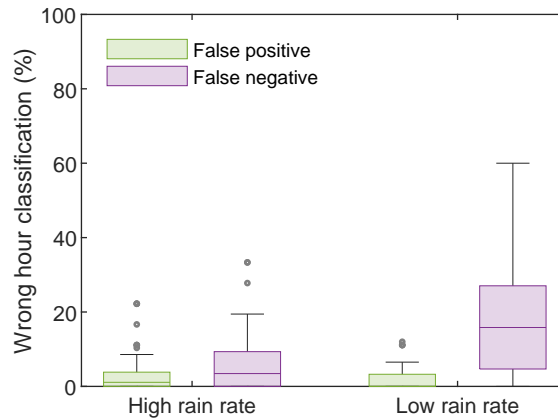
Figure 8. Percentage of hours subjected to wrong wet-dry classification (*false negative* or *false positive*), with respect to *high rain rate* and *low rain rate* events. The box plots display the median, the 0.25 (lower) and 0.75 (upper) quantiles, outliers (computed using the interquartile range), and the minimum and maximum values excluding any outliers.

and *false negative* hours in each of the 8 *high rain rate* events and for each of the 15 HRUs, as well as the two on the right were built from 60 values, the percentages related to the 4 *low rain rate* events in each HRU. For example, the maximum percentage of false negatives is 60%, which corresponds to HRU 2 during the *low rain rate* event 7 of Table 1. From a general point of view *low rain rate* events exhibit a higher median and a larger dispersion of *false negatives* than *high rain rate* events, whereas the occurrence of a *false positive* is relatively rare in both cases. These results confirm the inability of CMLs in detecting low rain rates, which depends on the quantization error issue discussed in Sec. 3.

Finally, in Fig. 9 we report box plots of ΔE values calculated for rainfall accumulated by each HRU over each of the 12 events. Again, the events are grouped in two classes according to rainfall intensity. The contrasting behaviour between *low rain rate* and *high rain rate* events is evident. In the former case, ΔE is mostly much lower than 0 and it is much more scattered. Once again, this result confirms that during *low rain rate* events, CMLs are not able to properly detect the lowest rainfall intensities. Regarding *high rain rate* events, there is not a clear trend. The median ΔE values are always within the range [-0.25,0.25] and their dispersion is low as well.

4.2 Comparison between RG- and CML-driven discharge simulations

In the following, discharge simulations obtained from three different data inputs (RGs, CMLs and CMLs+RGs) are assessed and compared with hydrographic measurements at Lesmo river section.

The output performances were evaluated with three indices: (1) the well-known Nash–Sutcliffe efficiency (NSE), (2) the relative error on peak discharge (REP) and (3) the relative error on flow volume (Dv). The last two indices are defined as
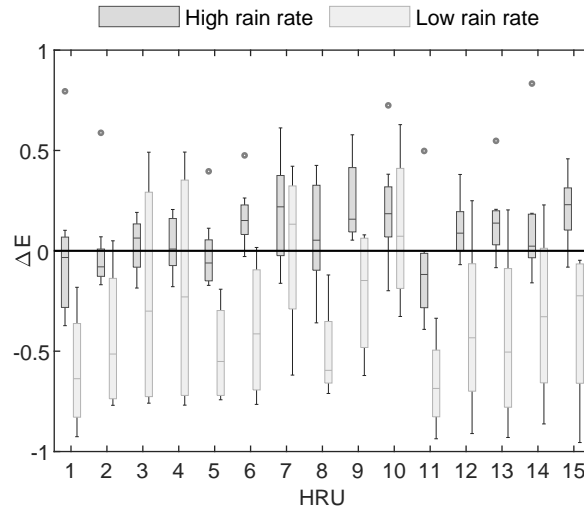
Figure 9. Box plots of ΔE in each HRU for the 12 storm events (divided in two groups according to rainfall intensity). The box plots display the median, the 0.25 (lower) and 0.75 (upper) quantiles, outliers (computed using the interquartile range), and the minimum and maximum values excluding any outliers.

follows:

$$\text{REP} = \frac{Q_{sim}^{max} - Q_{obs}^{max}}{Q_{obs}^{max}}; \tag{15}$$

365 $$\text{Dv} = \frac{V_{sim} - V_{obs}}{V_{obs}}, \tag{16}$$

where Q_{sim}^{max} is the simulated peak discharge, Q_{obs}^{max} is the observed peak discharge, V_{sim} is the simulated total flow volume, and V_{obs} is the observed total flow volume.

Performances of the 12 discharge simulations, grouped by rainfall data input, are summarized in Fig. 10, through box plots. The statistical dispersion (represented by the interquartile range) of CML-based discharge simulations are larger than RG-

370 based simulations. The use of CML data into the rainfall-runoff model seems to produce higher uncertainty. The combined use of RGs and CMLs instead decreases the statistical dispersion of results and leads to performances closer to those achieved through RG. Generally, CMLs exhibit worse performance than RGs in terms of NSE and Dv. As for REP, the two sets of sensors produce comparable errors of opposite sign, hence their combined use leads to an optimum value of the median error (0.06).

375 To gain a deeper understanding of the model performances on flow peaks, we produced a scatter plot of observed against simulated flow peaks in Fig. 11. The scatter plot firstly reveals that the best match between observations and simulations is not always achieved by RG-based simulations. In fact, for events 1, 3, 5, and 11 the optimum matching is given from CML- or
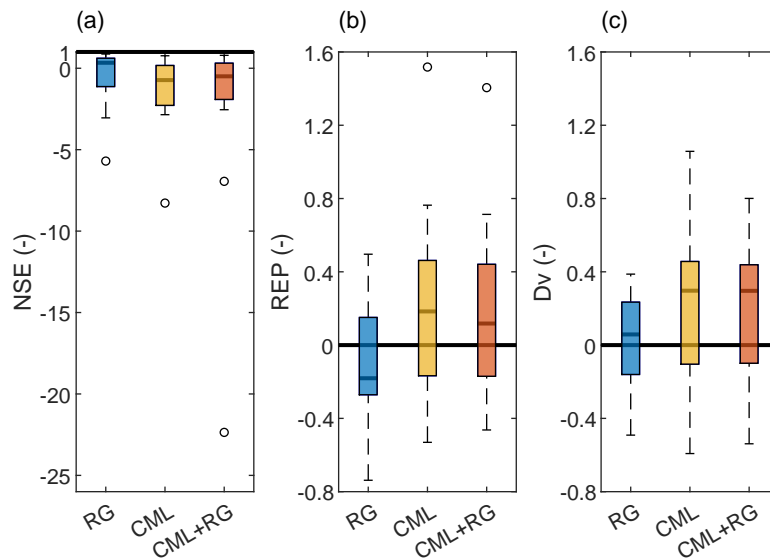
Figure 10. From panel (a) to (c), box plots of performance metrics, namely NSE, REP, and Dv, for the 12 selected flood events. The optimum values correspond to the bold black lines. The box plots display the median, the 0.25 (lower) and 0.75 (upper) quantiles, outliers (computed using the interquartile range), and the minimum and maximum values excluding any outliers.

CML+RG-based simulations. Moreover, the *low rain rate* events typically result in underestimated peak flow simulations with respect to the observations, considering either conventional or unconventional sensors, with an exception for event 5.

380   Figure 12 reports model inputs and outputs for events 5 and 2. We selected these two examples as they are characterized by a different meteorological configuration and lead to contrasting model performances. The first event is an autumn stratiform event, characterized by low rain intensity. In Fig. 12.a we can see that CML-based estimates in HRUs 1, 2, 5, 8, and 11 are quite low, with respect to RGs, due to the difficulties of CMLs in detecting light rain. In contrast, in the southern HRUs 10, 12, 13, 14, and 15, which have much more influence in the generation of river discharge, CML estimates are higher than RG

385   ones. Fig. 12.b shows an example where the CML-driven simulation better represents the observed outflow hydrograph, with respect to the RG-driven simulation. In particular, the best performance is gained when both the two types of rainfall sensors are used, and it provides an excellent Dv, equal to 0.03. The highest discrepancies between CML and RG estimates mostly involve the northern portion of the basin and have less impact in generating discharge. Event 2 is instead a typical intense convective summer event, characterized by a single rainfall peak. As rain rates are high all over the basin, contrary to event 5,

390   we observe in Fig. 12.c a better agreement between CML and RG estimates. River discharge simulations, reported in Fig. 12.d, are satisfactory, considering all the 3 input data. NSE values obtained respectively from RGs, CMLs, and RGs+CMLs data are 0.86, 0.77, and 0.80.
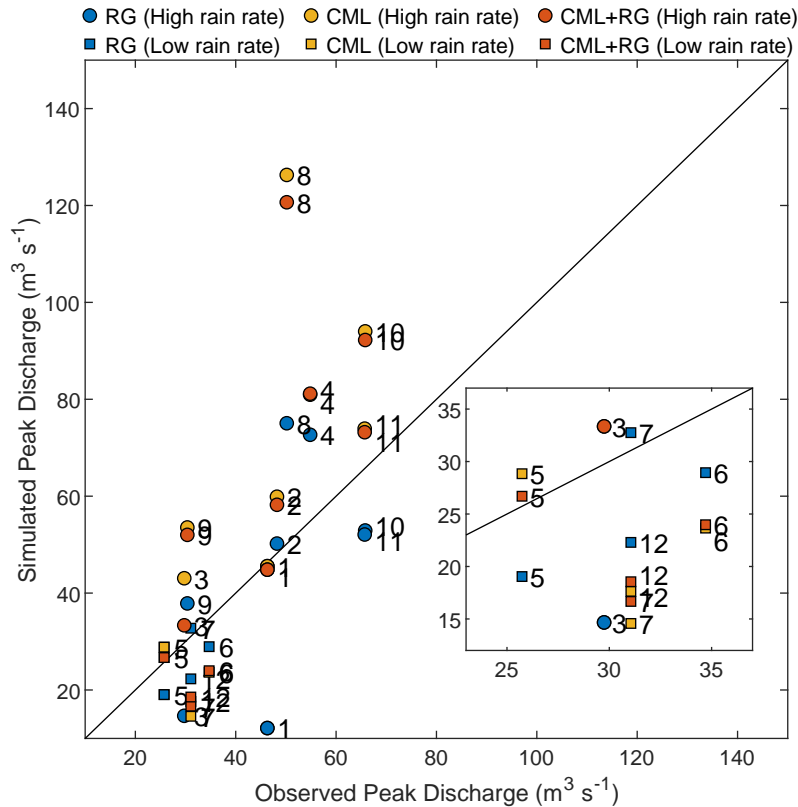
Figure 11. Observed peak flow against simulated one from RG (blue), CML (yellow), and CML+RG (orange). The two different markers, circles and squares, respectively stand for *high rain rate* and *low rain rate* events. Inset figure reports a zoom for events with a low peak discharge.

As the hydrological model has been calibrated with RG-detected rainfall data, it can be assumed that the best model performances are mostly achieved with RG data as input, as well. Unfortunately, we did not have at our disposal a database of CML events large enough to carry out a CML-based calibration. Nevertheless, we tried to overcome this problem, by recalibrating model parameters, with CML and CML+RG rainfall estimates as input, relying on the 12 available flood events. The same event-based calibration, was hence conducted using RG data as rainfall inputs. In such a way the comparison on discharge simulations may be led in a fair manner. We considered as optimum parameters those providing the highest median NSE values. Performance indices, subdivided by type of rainfall data input and type of calibration, are summarized in Fig. 13 by box plots. Please note that CML- and CML+RG-based calibrations improve the performance of the model when fed by unconventional input data. In particular, NSE values are comparable with the ones achieved by the use of RG data with a RG-based calibration. In fact, median NSE values for RG inputs with RG-based calibration, CML inputs with CML-based calibration, and CML+RG inputs with CML+RG-based calibration are 0.37, 0.35, and 0.38, respectively. For REP values we generally observe under-
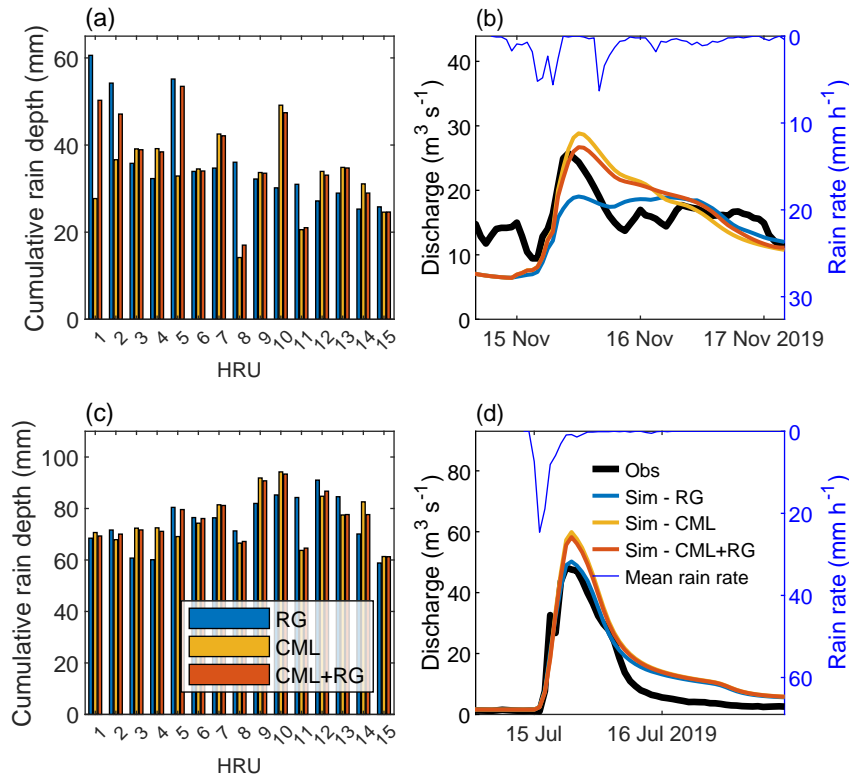
Figure 12. In panel (a) and (c), cumulative rainfall depth estimates from RG, CML, and CML+RG for storm/flood events 5 and 2, respectively. In panel (b) and (d) discharge observations and simulations gathered by using the three different input data, for the two same events.

estimations of the observed peak flow, considering CML- and CML+RG calibration but a smaller interquartile range when
405   compared with RG-based calibration. Concerning D_v values, performances for the CML- and CML+RG-based calibration are quite satisfactory, despite the combination providing the best performance is still RG inputs with RG-based calibration.
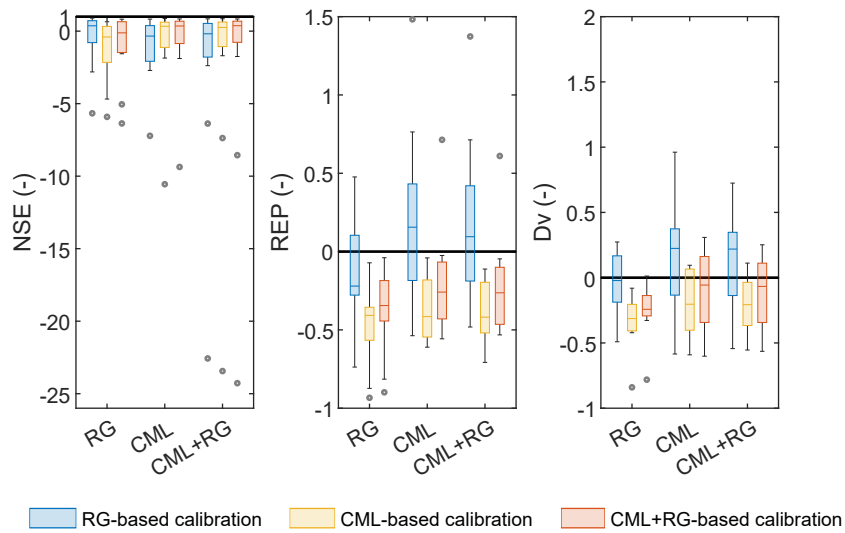
Figure 13. Box plots of the performance indices for the 12 flood events obtained with three different calibration sets (drawn in as many colours) and with three different input types (on the x-axis). The box plots display the median, the 0.25 (lower) and 0.75 (upper) quantiles, outliers (computed using the interquartile range), and the minimum and maximum values excluding any outliers.

5 Discussion

The analysis of interpolated rainfall data carried out in Sec. 4.1 reveals that CML and RG estimates of accumulated areal-averaged rainfall depths are comparable. However, two issues emerged.

First, CMLs exhibit a different behaviour depending on event intensity, since their sensitivity varies with length and frequency. Specifically, they return lower values of rainfall depth and rainfall accumulation in correspondence of *low rain rate* events. This aspect becomes evident either at different spatial scales (sub-basin and basin scales) and at different temporal scales (hourly and event-based time scales). In fact, due to a coarse quantization of the raw data, CMLs are not sensitive to low rain intensity, hence, when the rainfall depth value over a certain lapse of time is required (in our case 1 h), this limitation may lead to large errors, especially when light rain goes on for a long time. Despite some discrepancies in the behaviour of single CMLs with respect to their nearby RGs, as highlighted in Appendix A, we observed a good agreement between CML- and RG-based estimates in HRU centroids for high rain rates due to spatial interpolation which could mitigate such biases.

The second issue is the different CML density over the HRUs. It is well known that spatial interpolation methods are sensitive to sensor density (Xu et al., 2013), and consequently the relatively large distance of the available CMLs from the HRU centroids in the most scarcely populated areas (northern HRUs) may lead to loss of reliability of estimated rainfall depths. However, such an aspect appears to be less relevant when compared with the first one, at least when dealing with quite large HRUs (dozen of km^2). In fact, a careful comparison of Fig. 2 and Fig. 9 does not show an evident correlation between the mean CMLs-centroids distance and ΔE values.

Last but not least, model performances are influenced by the calibration process of model parameters. Similar model performances, in terms of NSE index, can be achieved with all the three types of input data (RGs, CMLs, and CMLs+RGs) if the calibration is carried out with the respective data inputs. This means that, after a proper calibration, opportunistic sensors could be exploited in semi-distributed hydrological models, as well as RGs. In particular we found that, after calibration, the set RGs+CMLs is the one providing the highest median NSE. However, it is worth highlighting that we calibrated the parameters on the basis of only 12 flood events. In order to assess a robust calibration and the associated validation, a larger data set of CML-based rainfall events should be processed.

5.1 Limitations and improvementes

One of the major difficulties encountered during analyses was the small amount of CML data, as we relied on only 458 hours of CML raw data grouped in 12 events. On the other hand, the database from RG observations was much more wider and we disposed of real-time data. An extension of the CML-based data set of events, or better yet, to have access to real-time CML raw data would definitely bring great benefits to the present work. Firstly, it would allow the development of a more robust statistical analysis on storm/flood events. Secondly, it would enable a proper calibration, and a validation as well, of the hydrological model based on CML data as rainfall input.

To enhance this work, it would also be useful to resort to the implementation of a CML-driven distributed model, which is expected to provide a more accurate description of the spatial variability of the precipitation field with respect to a semi-

distributed one. In such a case, the CML measurements would be better exploited by the use of advanced methods for spatial reconstruction of the rainfall field. For instance, techniques such as the tomographic reconstruction algorithm (D'Amico et al., 2016) or the stochastic reconstruction based on copulas (Haese et al., 2017; Salvadori et al., 2007), take advantage of the path integrated nature of CML measurements.

5.2 CML operational platforms

Although we showed that CML rainfall data can be successfully assimilated into hydrological models, their integration into real-time operational platforms (e.g. early warning systems) remains challenging. A number of aspects should be still considered including:

- generation of CML raw data formats suitable for rainfall estimation;

- real-time collection of raw data, which should be transparent to network operation;

- data transfer to a control center;

- non trivial data reduction process, especially if large sets of CMLs are managed.

The above mentioned issues suggest a systematic cooperation with mobile operators, who are the owners of CML network infrastructure.

5.3 New insights on Areal Reduction Factor

Up to now, we mainly investigated the exploitation of CML-based rainfall estimates with the purpose of testing their impact on the hydrological simulations of river discharge, with respect to the use of RG data. However, still important hydrological issues could be addressed by dealing with CML data. One of this is definitely the modelling of the Areal Reduction Factor (ARF), the factor which transforms a point rainfall for a given duration and return period into the areal average value for the same duration and return period (Natural Environmental Research Council (NERC), 1975). In last decades, great efforts have been put into the modelling of the ARF (De Michele et al., 2001), useful in the design of hydraulic and hydrological infrastructures, for flood risk evaluations, and rainfall threshold estimations in early warning systems (e.g., Kim et al., 2019; Biondi et al., 2021). As we dealt with a semi-distributed hydrological model we needed to transform point (from RG) and linear (from CML) precipitation measurements into areal values, over the HRU areas. Therefore, from a different perspective, this work could be also seen as a first step in order to test the modelling of ARF by using a combination of conventional and unconventional sensors.

6 Conclusions

In this work, we assessed the use of commercial microwave links (CMLs) as opportunistic rainfall sensors within the hydrological modelling. We focused on Lambro, a peri-urban catchment, $260 \ \mathrm{km}^2$ in area, located north of Milan (Italy) and covered by 50 CMLs that are part of the network owned by a major mobile operator. Lambro's area is covered by 13 rain gauges

(RGs) as well, which we used both as an independent rainfall data set and in combination with CMLs. We implemented a semi-distributed hydrological model and carried out two types of comparison between CML and RG data. First, we considered rainfall data (hourly rainfall depths, the input of the hydrological model, and total accumulations at the storm end, for a sample of 12 storm events) interpolated at the HRU centroids. Then, we compared river discharge simulations (model output) from RGs, CMLs and RGs+CMLs against flow measurements.

Concerning the comparison of the two sources of rainfall data, we found out that high intensity events detected by CMLs are in accordance with RG measurements. On the other hand we came across a critical aspect, which is the inability of CMLs to detect low rain rates, due to the coarse 1 dB quantization step of raw data (i.e. received power levels). The minimum detectable rainfall intensity depends on the operation frequency of CMLs as well as on their length, and, for the available set of CMLs, it ranges from 1 mm h^{-1} to 10 mm h^{-1}. Such a limitation results in the underestimation of rainfall depths interpolated in the HRU centroids for low intensity storm events, when compared to RG-based rainfall data.

The hydrographs simulated by the hydrological model perform better in terms of Nash-Sutcliffe efficiency, NSE, and relative error on flow volume, Dv, in the case of RGs rather than of CMLs. This result is not surprising as the model was calibrated using RG data throughout one year data. Nevertheless, satisfactory values of relative error on peak discharge, REP, are achieved through the use of CML and CML+RG data as inputs into the RG-based calibrated model.

By calibrating the model with CML data and by using the same as input, it is possible to improve the model performance, which becomes comparable with the case of RG-calibration and RG-input. Even a slightly better performance can be gathered with a CML+RG-based calibration and CML+RG data as input.

Despite the lack of sensitivity of the CMLs which we relied on, this analysis proves that rainfall estimates based on CMLs could be exploited in hydrology, with a certain confidence, for river discharge simulations. These results show that the use of opportunistic sensors could support hydrological modelling, especially in those areas lacking traditional monitoring systems. Furthermore, in the regions already equipped with traditional rainfall sensors, the integration of them with CMLs could bring advantages for hydrological applications as well, as this increases the number of reliable rainfall measurements.

7 Data availability

Meteorological and hydrological data from the Hydrographic Office of ARPA Lombardia are openly available at https://www.arpalombardia.it. Commercial Microwave Links data are available from the authors with the permission of Vodafone Italia S.p.A..

Author contributions. C.D.M., R.N., M.D.A., A.G. made the conceptualization; R.N. handled CML data; G.C. handled gauge data, G.C., C.D., C.D.M. developed the hydrological model; G.C. made the model calibrations and validations; G.C. prepared Figs. 1-2, 5-13, and A1; R.N. prepared Figs.3 and 4; G.C. wrote the first draft of the manuscript; all the authors reviewed the manuscript.

Competing interests. All authors declare that they have no conflicts of interest.

500 *Acknowledgements.* We wish to acknowledge the support by Fondazione CARIPLO through the MOPRAM project (http://www.mopram.it). We thank ARPA Lombardia for providing us with meteorological and hydrological data.

Appendix A: Local comparison between CML and RG rainfall time series

Rainfall amounts collected from CMLs and RGs are here compared through an analysis of the corresponding time series. To this aim, we selected four CMLs having at least one RG within 5 km, as done for the scatter plots of Fig. 4 and we plotted the
505 CMLs and RGs time series of rainfall intensity and cumulative rainfall depth during the storm events 7, 8, 9 and 10 of Table 1. Please note that rainfall intensity is obtained from slightly different resolution times, i.e. 15 min for CMLs and 10 min for RGs, respectively. Fig. A1 shows the results. The differences between individual CMLs and nearby RGs are not surprising, due to three main factors: (1) the different nature of the sensors, (2) the CMLs were not calibrated using other rainfall sensors as weather radars, and (3) the relative position between CML and RG. What is mostly evident are the differences between the low
510 (event 7) and the high intensity events (events 8, 9, and 10). In the former case, the CMLs miss most of rainfall occurrences, causing a large underestimation of the rainfall accumulated at the end of the event. During event 7, RGs detected rain intensities from 1 up to 6 mmh^{-1}. The last value is approximately the minimum detectable rain intensity for the CML with lowest frequencies (in Fig. A1.a). However, it is worth to underline that such an underestimating behaviour is observable not only for short and low-frequency CMLs but also for the most sensitive ones. In fact, large underestimations are reported in panels (k),
515 (l), and (q) which are related to links with minimum detectable rain intensity equal to 1.6, 1.4, and 1 mmh^{-1}, respectively. This systematic underestimating behaviour also impact estimates of rainfall depths at the basin and sub-basin scale, as shown by results in Sec. 4.1. The three *high rain rate* events highlight different behaviours depending on the considered CML and its relative location respect to the RGs. The short and low frequency CML, given in panel (a), shows quite large discrepancy with its nearby RG, regarding to either the peaks timing or the total observed rainfall depth, and reveals both underestimating and
520 overestimating behaviours (see panels (c)-(e) of Fig. A1). The performances of the two medium-length and medium-frequency CMLs (second row panels (h)-(j) and third row panels (m)-(o) of Fig. A1) are in mutual agreement and are definitely better with respect to the case shown in the first row (see panels (c)-(e) of Fig. A1). Specifically, it can be noticed that in most of the cases these two CMLs well reproduce the highest peaks observed by the closest RGs, which are also those located right next to their middle point. However, they show some discrepancies (lower values with respect to RGs) as the rain rate decreases. This
525 behaviour is particularly evident in panels (i) and (n), for event 9. Finally, the highest-frequency CML (fourth row in Fig. A1) exhibits different performances during the three *high rain rate* events (panels (r)-(t)). For example, at odds with the previous cases, in event 10, the CML tends to overestimate the lowest rain rates, leading to a large overestimation (up to 60%) of the cumulated rainfall depth. In this case, the differences between CML and RGs could be also due to the not-optimal relative location between CML and RGs. Results reported in Sec. 4.1 show that interpolating several CML data at HRU centroids

530   mitigates the inaccuracy of individual CMLs and leads to acceptable estimates of the flow except in the case of low intensity events due to their limited sensitivity.
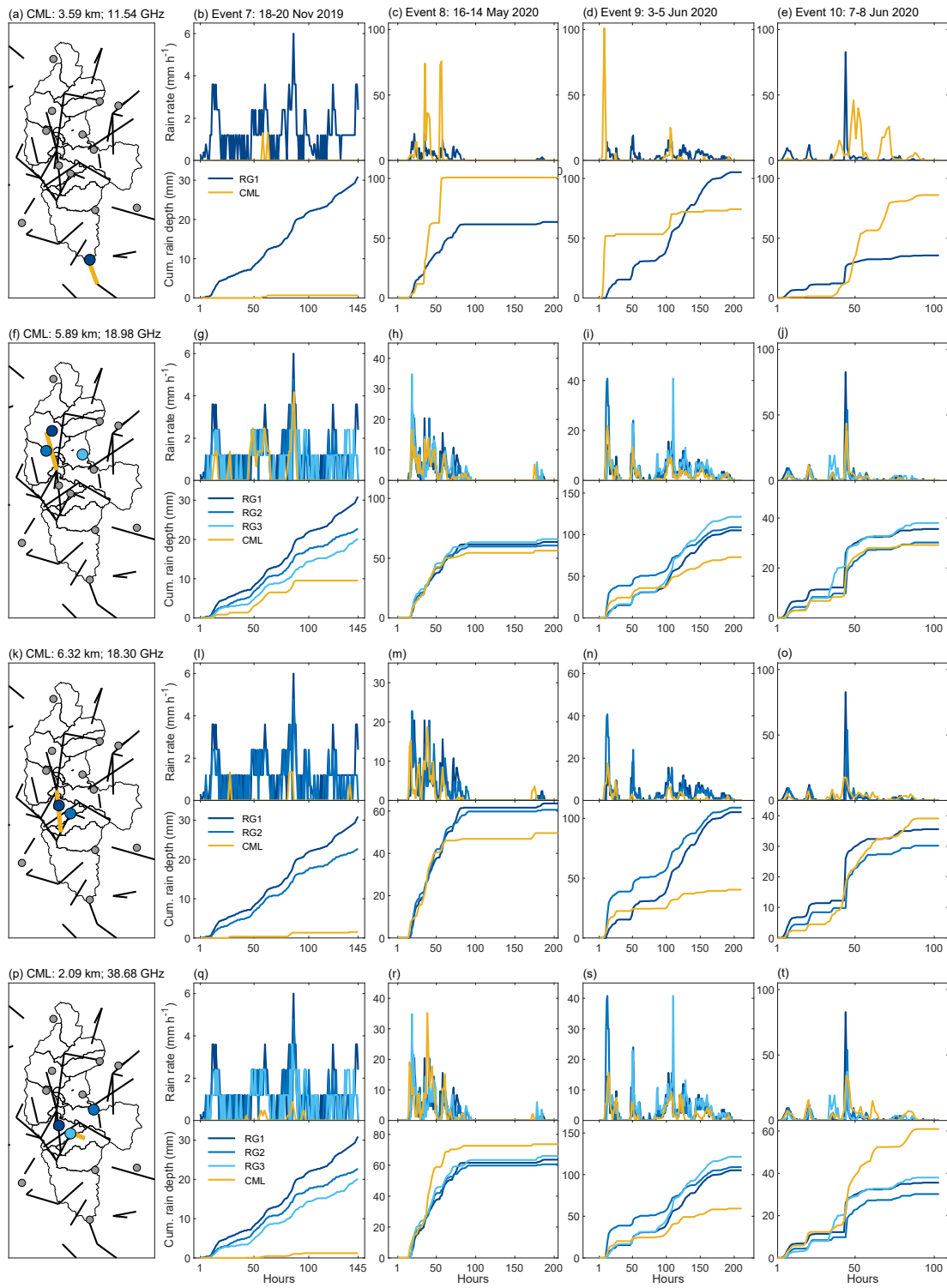
Figure A1. Comparison between single CML and nearby RGs. Each row shows (1) the location over the Lambro basin of the selected CML and its nearby RGs, (2) the CML-RGs comparison on rain rate time series, and (3) the CML-RGs comparison on cumulated rainfall depths.

References

Alberoni, P., Andersson, T., Mezzasalma, P., Michelson, D., and Nanni, S.: Use of the vertical reflectivity profile for identification of anomalous propagation, Meteorol. Appl., 8, 257–266, https://doi.org/10.1017/S1350482701003012, 2001.

Arnaud, P., Lavabre, J., Fouchier, C., Diss, S., and Javelle, P.: Sensitivity of hydrological models to uncertainty in rainfall input, Hydrol. Sci. J., 56, 397–410, https://doi.org/10.1080/02626667.2011.563742, 2011.

Atlas, D. and Ulbrich, C. W.: Path-and area-integrated rainfall measurement by microwave attenuation in the 1–3 cm band, Journal of Applied Meteorology and Climatology, 16, 1322–1331, https://doi.org/10.1175/1520-0450(1977)016<1322:PAAIRM>2.0.CO;2, 1977.

Bárdossy, A. and Das, T.: Influence of rainfall observation network on model calibration and application, Hydrol. Earth Syst. Sci., 12, 77–89, https://doi.org/10.5194/hess-12-77-2008, 2008.

Bengtsson, L.: Daily and hourly rainfall distribution in space and time–conditions in southern Sweden, Hydrol. Res., 42, 86–94, https://doi.org/10.2166/nh.2011.080b, 2011.

Bingner, R. L. and Theurer, F. D.: AnnAGNPS: technical description, Tech. rep., US Dept Agriculture, Agricultural Research Services, 2005.

Biondi, D., Greco, A., and De Luca, D. L.: Fixed-area vs storm-centered Areal Reduction factors: a Mediterranean case study, J. Hydrol., 595, 125 654, https://doi.org/10.1016/j.jhydrol.2020.125654, 2021.

Brauer, C. C., Overeem, A., Leijnse, H., and Uijlenhoet, R.: The effect of differences between rainfall measurement techniques on groundwater and discharge simulations in a lowland catchment, Hydrol. Processes, 30, 3885–3900, https://doi.org/10.1002/hyp.10898, 2016.

Brooks, R. H. and Corey, A. T.: Hydraulic properties of porous media, Fort Collins, Colorado State University, CO, USA, 1964.

Chen, D., Ou, T., Gong, L., Xu, C.-Y., Li, W., Ho, C.-H., and Qian, W.: Spatial interpolation of daily precipitation in China: 1951–2005, Adv. Atmos. Sci., 27, 1221–1232, https://doi.org/10.1007/s00376-010-9151-y, 2010.

Chen, J.-Y., Trömel, S., Ryzhkov, A., and Simmer, C.: Assessing the benefits of specific attenuation for quantitative precipitation estimation with a C-band radar network, Journal of Hydrometeorology, 22, 2617–2631, https://doi.org/10.1175/JHM-D-20-0299.1, 2021.

Chwala, C. and Kunstmann, H.: Commercial microwave link networks for rainfall observation: Assessment of the current status and future challenges, Wiley Interdiscip. Rev.: Water, 6, e1337, https://doi.org/10.1002/wat2.1337, 2019.

Cugerone, K. and De Michele, C.: Johnson SB as general functional form for raindrop size distribution, Water Resour. Res., 51, 6276–6289, https://doi.org/10.1002/2014WR016484, 2015.

Dawdy, D. R. and Bergmann, J. M.: Effect of rainfall variability on streamflow simulation, Water Resour. Res., 5, 958–966, https://doi.org/10.1029/WR005i005p00958, 1969.

De Michele, C., Kottegoda, N. T., and Rosso, R.: The derivation of areal reduction factor of storm rainfall from its scaling properties, Water Resources Research, 37, 3247–3252, https://doi.org/https://doi.org/10.1029/2001WR000346, 2001.

de Simas, M. J. C.: Lag-time characteristics in small watersheds in the United States, UMI, Ann Arbor, MI, USA, 1996.

Delhomme, J. P.: Kriging in the hydrosciences, Adv. Water Resour., 1, 251–266, https://doi.org/10.1016/0309-1708(78)90039-8, 1978.

Dooge, J.: Linear theory of hydrologic systems, 1468, Agricultural Research Service, US Department of Agriculture, 1973.

D'Amico, M., Manzoni, A., and Solazzi, G. L.: Use of operational microwave link measurements for the tomographic reconstruction of 2-D maps of accumulated rainfall, IEEE Geosci. Remote Sens. Lett., 13, 1827–1831, https://doi.org/10.1109/LGRS.2016.2614326, 2016.

Eshel, A., Messer, H., Kunstmann, H., Alpert, P., and Chwala, C.: Quantitative analysis of the performance of spatial interpolation methods for rainfall estimation using commercial microwave links, J. Hydrometeor., 22, 831–843, https://doi.org/10.1175/JHM-D-20-0164.1, 2021.

EU Water Directors: Best Practices on flood prevention, protection and mitigation, in: Meetings in Budapest on 30 November and 1 December 2002, and in Bonn on 5/6 February 2003., http://ec.europa.eu/environment/water/flood_risk/pdf/flooding_bestpractice.pdf, 2003.

Fencl, M., Rieckermann, J., Schleiss, M., Stránskỳ, D., and Bareš, V.: Assessing the potential of using telecommunication microwave links in urban drainage modelling, Water Sci. Technol., 68, 1810–1818, https://doi.org/IWA 10.2166/wst.2013.429, 2013.

Fenicia, F., Pfister, L., Kavetski, D., Matgen, P., Iffly, J.-F., Hoffmann, L., and Uijlenhoet, R.: Microwave links for rainfall estimation in an urban environment: Insights from an experimental setup in Luxembourg-City, J. Hydrol., 464–465, 69–78, https://doi.org/10.1016/j.jhydrol.2012.06.047, 2012.

Ferro, V.: Riqualificazione ambientale dei corsi d'acqua, Quaderni di Idronomia Montana, Nuova Editoriale Bios, 2006.

Giuli, D., Toccafondi, A., Gentili, G. B., and Freni, A.: Tomographic reconstruction of rainfall fields through microwave attenuation measurements, J. Appl. Meteorol. Climatol., 30, 1323–1340, https://doi.org/10.1175/1520-0450(1991)030<1323:TRORFT>2.0.CO;2, 1991.

Graf, M., Chwala, C., Polz, J., and Kunstmann, H.: Rainfall estimation from a German-wide commercial microwave link network: optimized processing and validation for 1 year of data, Hydrol. Earth Syst. Sci., 24, 2931–2950, https://doi.org/10.5194/hess-24-2931-2020, 2020.

Haese, B., Hörning, S., Chwala, C., Bárdossy, A., Schalge, B., and Kunstmann, H.: Stochastic reconstruction and interpolation of precipitation fields using combined information of commercial microwave links and rain gauges, Water Resour. Res., 53, 10 740–10 756, https://doi.org/10.1002/2017WR021015, 2017.

Hargreaves, G. H. and Samani, Z. A.: Reference crop evapotranspiration from temperature, Appl. Eng. Agr., 1, 96–99, https://doi.org/10.13031/2013.26773, 1985.

Ignaccolo, M. and De Michele, C.: One, No One, and One Hundred Thousand: The Paradigm of the Z–R Relationship, J. Hydrometeorol., 21, 1161–1169, https://doi.org/10.1175/JHM-D-19-0177.1, 2020.

ITU-R P.838-3: Specific attenuation model for rain for use in prediction methods, Tech. rep., 2005.

Jaffrain, J., Studzinski, A., and Berne, A.: A network of disdrometers to quantify the small-scale variability of the raindrop size distribution, Water Resour. Res., 47, https://doi.org/10.1029/2010WR009872, 2011.

Jameson, A. R. and Kostinski, A.: Spurious power–law relations among rainfall and radar parameters, Q. J. R. Meteorolog. Soc., 128, 2045–2058, https://doi.org/10.1256/003590002320603520, 2002.

Kidd, C. and Huffman, G.: Global precipitation measurement, Meteorol. Appl., 18, 334–353, https://doi.org/10.1002/met.284, 2011.

Kim, J., Lee, J., Kim, D., and Kang, B.: The role of rainfall spatial variability in estimating areal reduction factors, J. Hydrol., 568, 416–426, https://doi.org/10.1016/j.jhydrol.2018.11.014, 2019.

Köppen, W. P.: Die Klimate der Erde: Grundriss der Klimakunde, Geogr. J., 65, 1925.

Lombardi, G., Ceppi, A., Ravazzani, G., Davolio, S., and Mancini, M.: From Deterministic to Probabilistic Forecasts: The 'Shift-Target' Approach in the Milan Urban Area (Northern Italy), Geosciences, 8, 181, https://doi.org/10.3390/geosciences8050181, 2018.

Luini, L., Roveda, G., Zaffaroni, M., Costa, M., and Riva, C.: The Impact of Rain on Short E-Band Radio Links for 5G Mobile Systems: Experimental Results and Prediction Models, IEEE Trans. Antennas Propag., 68, 3124–3134, https://doi.org/10.1109/TAP.2019.2957116, 2020.

Maidment, D.: Handbook of hydrology, McGraw-Hill, New York, NY, USA, 1993.

Marshall, J. S. and Palmer, W. M.: The distribution of raindrops with size, J. Meteorol., 5, 165–166, https://doi.org/10.1175/1520-0469(1948)005, 1948.

605 Masseroni, D., Cislaghi, A., Camici, S., Massari, C., and Brocca, L.: A reliable rainfall–runoff model for flood forecasting: review and application to a semi-urbanized watershed at high flood risk in Italy, Hydrol. Res., 48, 726–740, https://doi.org/10.2166/nh.2016.037, 2017.

Messer, H., Zinevich, A., and Alpert, P.: Environmental monitoring by wireless communication networks, Science, 312, 713–713, https://doi.org/10.1126/science.1120034, 2006.

610 Met Office: Fact Sheet No. 3: Water in the Atmosphere, Tech. rep., 2007.

Mockus, V.: Use of storm and watershed characteristics in synthetic unit hydrograph analysis and application, US Soil Conservation Service, 1957.

Moriasi, D. N., Arnold, J. G., Van Liew, M. W., Bingner, R. L., Harmel, R. D., and Veith, T. L.: Model evaluation guidelines for systematic quantification of accuracy in watershed simulations, Transactions of the ASABE, 50, 885–900, https://doi.org/10.13031/2013.23153, 615 2007.

Myers, D. E.: Co-kriging—New developments, in: Geostatistics for natural resources characterization, pp. 295–305, Springer, 1984.

Nash, J. E. and Sutcliffe, J. V.: River flow forecasting through conceptual models part I – A discussion of principles, J. Hydrol., 10, 282–290, https://doi.org/10.1016/0022-1694(70)90255-6, 1970.

Natural Environmental Research Council (NERC): Flood studies report, vol. II, Tech. rep., Meteorological studies, Swindon, England, 1975.

620 Nebuloni, R., D'Amico, M., Cazzaniga, G., and De Michele, C.: On the Use of Minimum and Maximum Attenuation for Retrieving Rainfall Intensity Through Commercial Microwave Links, URSI Radio Sci. Lett., 2, https://doi.org/10.46620/20-0062, 2020.

New, M., Todd, M., Hulme, M., and Jones, P.: Precipitation measurements and trends in the twentieth century, Int. J. Climatol., 21, 1889–1922, https://doi.org/10.1002/joc.680, 2001.

Obled, C., Wendling, J., and Beven, K.: The sensitivity of hydrological models to spatial rainfall patterns: an evaluation using observed data, 625 J. Hydrol., 159, 305–333, https://doi.org/10.1016/0022-1694(94)90263-1, 1994.

Overeem, A., Leijnse, H., and Uijlenhoet, R.: Country-wide rainfall maps from cellular communication networks, Proc. Natl. Acad. Sci., 110, 2741–2745, https://doi.org/10.1073/pnas.1217961110, 2013.

Overeem, A., Leijnse, H., and Uijlenhoet, R.: Retrieval algorithm for rainfall mapping from microwave links in a cellular communication network, Atmospheric Measurement Techniques, 9, 2425–2444, https://doi.org/10.5194/amt-9-2425-2016, https://amt.copernicus. 630 org/articles/9/2425/2016/, 2016.

Parkes, B., Wetterhall, F., Pappenberger, F., He, Y., Malamud, B., and Cloke, H.: Assessment of a 1-hour gridded precipitation dataset to drive a hydrological model: a case study of the summer 2007 floods in the Upper Severn, UK, Hydrol. Res., 44, 89–105, https://doi.org/10.2166/nh.2011.025, 2013.

Pastorek, J., Fencl, M., Rieckermann, J., and Bareš, V.: Commercial microwave links for urban drainage modelling: The effect of link char-635 acteristics and their position on runoff simulations, J. Environ. Manage., 251, 109 522, https://doi.org/10.1016/j.jenvman.2019.109522, 2019.

Raghavan, S.: Radar Meteorology, Springer, 2013.

Rahimi, A., Holt, A., Upton, G., and Cummings, R.: Use of dual-frequency microwave links for measuring path-averaged rainfall, Journal of Geophysical Research: Atmospheres, 108, 4467, https://doi.org/10.1029/2002JD003202, 2003.

640 Rauber, R. M. and Nesbitt, S. W.: Radar meteorology: A first course, John Wiley & Sons, Glasgow, UK, 2018.

Ravazzani, G., Mancini, M., Giudici, I., and Amadio, P.: Effects of soil moisture parameterization on a real-time flood forecasting system based on rainfall thresholds, in: Quantification and Reduction of Predictive Uncertainty for Sustainable Water Resources Management, Proc. Symposium HS 2004 at IUGG 2007, pp. 407—-416, IAHS Publ., Perugia, 2007.

645 Ravazzani, G., Bocchiola, D., Groppelli, B., Soncini, A., Rulli, M. C., Colombo, F., Mancini, M., and Rosso, R.: Continuous streamflow simulation for index flood estimation in an Alpine basin of northern Italy, Hydrological Sciences Journal, 60, 1013–1025, https://doi.org/10.1080/02626667.2014.916405, 2015.

Ravazzani, G., Amengual, A., Ceppi, A., Homar, V., Romero, R., Lombardi, G., and Mancini, M.: Potentialities of ensemble strategies for flood forecasting over the Milano urban area, J. Hydrol., 539, 237–253, https://doi.org/10.1016/j.jhydrol.2016.05.023, 2016.

Roversi, G., Alberoni, P. P., Fornasiero, A., and Porcù, F.: Commercial microwave links as a tool for operational rainfall monitoring in

650 Northern Italy, Atmos. Meas. Tech., 13, 5779–5797, https://doi.org/10.5194/amt-13-5779-2020, 2020.

Salvadori, G., De Michele, C., Kottegoda, N. T., and Rosso, R.: Extremes in nature: an approach using copulas, vol. 56, Springer, Dordrecht, The Netherlands, 2007.

Schleiss, M. and Berne, A.: Identification of dry and rainy periods using telecommunication microwave links, IEEE Geoscience and Remote Sensing Letters, 7, 611–615, 2010.

655 Schleiss, M., Rieckermann, J., and Berne, A.: Quantification and modeling of wet-antenna attenuation for commercial microwave links, IEEE Geosci. Remote Sens. Lett., 10, 1195–1199, 2013.

Shepard, D.: A two-dimensional interpolation function for irregularly-spaced data, in: Proceedings of the 1968 23rd ACM national conference, pp. 517–524, ACM, New York, NY, USA, https://doi.org/10.1145/800186.810616, 1968.

Smiatek, G., Keis, F., Chwala, C., Fersch, B., and Kunstmann, H.: Potential of commercial microwave link network derived rainfall for river

660 runoff simulations, Environ. Res. Lett., 12, 034 026, https://doi.org/10.1088/1748-9326/aa5f46/meta, 2017.

Stransky, D., Fencl, M., and Bares, V.: Runoff prediction using rainfall data from microwave links: Tabor case study, Water Sci. Technol., 2017, 351–359, https://doi.org/10.2166/wst.2018.149, 2018.

Thiessen, A. H.: Precipitation averages for large areas, Monthly weather review, 39, 1082–1089, https://doi.org/10.1175/1520-0493(1911)39<1082b:PAFLA>2.0.CO;2, 1911.

665 US Department of Agriculture Soil Conservation Service: National Engineering Handbook, section 4 - Hydrology, Washington, DC, USA, 1985.

Xie, P., Rudolf, B., Schneider, U., and Arkin, P. A.: Gauge-based monthly analysis of global land precipitation from 1971 to 1994, J. Geophys. Res.: Atmos., 101, 19 023–19 034, https://doi.org/10.1029/96JD01553, 1996.

Xu, H., Xu, C.-Y., Chen, H., Zhang, Z., and Li, L.: Assessing the influence of rain gauge density and distribution on hydrological model

670 performance in a humid region of China, J. Hydrol., 505, 1–12, https://doi.org/10.1016/j.jhydrol.2013.09.004, 2013.

Younger, P. M., Freer, J. E., and Beven, K. J.: Detecting the effects of spatial variability of rainfall on hydrological modelling within an uncertainty analysis framework, Hydrol. Processes, 23, 1988–2003, https://doi.org/10.1002/hyp.7341, 2009.

Zhang, G., Mahale, V. N., Putnam, B. J., Qi, Y., Cao, Q., Byrd, A. D., Bukovcic, P., Zrnic, D. S., Gao, J., Xue, M., et al.: Current status and future challenges of weather radar polarimetry: Bridging the gap between radar meteorology/hydrology/engineering and numerical

675 weather prediction, Adv. Atmos. Sci., 36, 571–588, https://doi.org/10.1007/s00376-019-8172-4, 2019.